Available online at www.sciencedirect.com
ScienceDirect
Trans. Nonferrous Met. Soc. China 35(2025) 2903−2917
Transactions of Nonferrous Metals Society of China
www.tnmsc.cn

Angular deviations and influential factors of Burgers orientation relationship during $\beta\rightarrow\alpha$ phase transformation in titanium alloys

Ming-bing LI[1,2*], Kai WANG[1*], Bin WANG[1], Chao LV[1],
Xin-nan WANG[2], Xing LI[3], Zhi-shou ZHU[2], Hui-long HOU[1,4], Xin-qing ZHAO[1]

1. School of Materials Science and Engineering, Beihang University, Beijing 100191, China;
2. Key Laboratory of Advanced Titanium Alloys, Beijing Institute of Aeronautical Materials, Aero Engine Corporation of China, Beijing 100095, China;
3. MIIT Key Laboratory of Advanced Metallic and Intermetallic Materials Technology, Nanjing University of Science and Technology, Nanjing 210094, China;
4. Tianmushan Laboratory (Zhejiang Provincial Laboratory for Aviation), Hangzhou 311312, China

Received 15 January 2024; accepted 3 September 2024

Abstract: The angular deviations and influential factors of Burgers orientation relationship (BOR) in Ti−6Al−4V and Ti−6.5Al−2Zr−1Mo−1V alloys were investigated by optical microscope (OM), scanning electron microscope (SEM), electron backscattered diffraction (EBSD) and high-angle annular dark-field scanning transmission electron microscope (HAADF-STEM). A spherical center angle model was introduced to calculate the angular deviations from the ideal BOR between α and β phases. The results indicate that α and β phases in α colonies of both alloys do not follow the perfect BOR during $\beta\rightarrow\alpha$ phase transformation, with angular deviation values less than 3°. Through detailed microstructure characterization, the broad face of α/β interfaces viewed along two different electron incident directions shows the atomic-scale terrace-ledge structure, and many dislocations are observed within α and β phases and near α/β interfaces. Further studies reveal that the angular deviations mainly originate from lattice distortions caused by dislocations in α and β phases and lattice mismatches at α/β interfaces.

Key words: titanium alloy; Burgers orientation relationship; angular deviation; α/β interface; dislocation; lattice distortion

1 Introduction

Titanium and its alloys exhibit two common phases, namely β and α phases, which possess body-centered cubic (BCC) and hexagonal close-packed (HCP) crystal structures, respectively [1,2]. In fact, β phase dominates at elevated temperatures and gradually transforms into α phase by diffusion-controlled phase transformation as temperature decreases. Previous studies [3−6] demonstrated that the orientation of β and α phases follows the Burgers orientation relationship (BOR), i.e., $\{110\}_\beta // \{0001\}_\alpha$ and $\langle 111\rangle_\beta // \langle 11\bar{2}0\rangle_\alpha$, as schematically shown in Figs. 1(a) and (b). Theoretically, there are 12 equivalent α variants that follow the BOR during $\beta\rightarrow\alpha$ phase transformation [7,8]. As a matter of fact, α and β phases may not follow the ideal BOR during phase transformation in real materials. Taking the pole figures (PFs) of titanium alloy shown in Fig. 1(c) as an example, the position of one pole in $(110)_\beta$ PF overlaps with the position of

* Ming-bing LI and Kai WANG contributed equally to this work
Corresponding author: Zhi-shou ZHU, Tel: +86-13501067682, E-mail: zhuzzs@126.com;
Hui-long HOU, Tel: +86-13121866116, E-mail: huilong_hou@buaa.edu.cn
https://doi.org/10.1016/S1003-6326(25)66856-7

one pole in $(0001)_\alpha$ PF (indicated by black arrow), as well as in $(111)_\beta$ and $(11\bar{2}0)_\alpha$ PFs, which demonstrates that the two phases follow the BOR in general. However, all poles in PFs illustrated in Fig. 1(c) show a dispersed distribution, suggesting a possible deviation from the ideal BOR.

In practice, α phases can be classified into primary α phase (α_p), grain boundary α phase α_{GB}, and α colonies according to their geometrical arrangements in microstructure [1]. Specifically, α_p phase is typically observed as sphere-like particles embedded in transformed β matrix. The formation of α_p phase usually includes two stages: (1) dynamic globularization of α plates during hot deformation; (2) static globularization of deformed α plates during heat treatment [9−11]. There is still debate over whether α_p phase maintains the BOR with its neighboring β phase [12,13]. For example, it was found that only a small portion of α_p phase followed the BOR with adjacent β phase, and most of α_p phase exhibited angular deviations from the perfect BOR [13]. α_{GB} phase usually nucleates and develops at the prior β grain boundaries by $\beta\rightarrow\alpha$ phase transformation [1,14]. In most cases, α_{GB} phase holds the BOR with one of the two neighboring β grains and has a small deviation from the BOR to another β grain [15−17]. The α colonies nucleate either at the interfaces of α_{GB} or at the prior β grain boundaries during slow cooling and grow into parallel α plates with the same crystallographic orientation within the β grain [1,2,14]. Numerous experimental investigations [8,16,18,19] demonstrated that α and β phases in α colonies obeyed the BOR, and only a limited number of α colony variants were typically found in β grains because of variant selection. In view of the nature of transformation for α phases mentioned above, α colonies are suitable for investigating whether α and β phases follow the ideal BOR during $\beta\rightarrow\alpha$ phase transformation.

Early study revealed that a spread of ~5.0° around the BOR had to be taken into account to relate the inherited orientations to the parent one during $\alpha\rightarrow\beta\rightarrow\alpha$ phase transformation in cold-rolled pure titanium [19]. However, angular deviation from the ideal BOR within 8.0° was introduced to identify whether α_p and β phases obeyed the BOR in TA12A titanium alloy [13]. Another study revealed that the orientation relationships (ORs) between α precipitates and β matrix phase could be grouped into 3 independent ORs, and all ORs were close to the ideal BOR in Ti−5.26Cr alloy [20]. To measure the deviations of OR between α_{GB} and neighboring β grain, which do not obey the BOR, the misorientation angle θ_m (double-BOR criterion) was initially introduced by SHI et al [16]. They found that α_{GB} phase could maintain the BOR with two adjacent β grains when θ_m was less than 15.0° in Ti-5553 alloy. Subsequently, LIU et al [21] revealed that α_{GB} maintained the BOR with two neighboring β grains when θ_m was less than 10.0° in Ti-17 alloy. This conclusion had also been followed to study the specific GBs at the triple junction of β grains that might obey the double-BOR criterion in TB8 alloy [22]. However, previous studies [6,16,20−22] ignored the possible angular deviations from the ideal BOR between the two phases, and more importantly, the deviations were observed to significantly affect the crystallographic orientation and morphology of α phase. In the present study, we investigated the angular deviations of BOR in α colonies of Ti−6Al−4V and Ti−6.5Al−2Zr−1Mo−1V alloys and explored the mechanisms contributing to the deviations. The results help to gain a deeper understanding of the crystallographic orientation evolution during $\beta\rightarrow\alpha$ phase transformation and provide a reference for optimizing the microstructures of titanium alloys.

2 Calculation method and experiment

2.1 Calculation method

The stereographic projection is a method of projecting a three-dimensional unit cell onto a two-dimensional projection. Angular relationships between different planes or directions in crystal structure can be easily obtained in the two-dimensional projection [23]. Assume two HCP and BCC unit cells, which are small enough to be treated as point O, as shown in Fig. 1(d). A large sphere, called a reference sphere, is then constructed with point O as the center. To obtain $(0001)_\alpha$ pole stereographic projection concerning HCP unit cell, we draw line OA perpendicular to $(0001)_\alpha$ plane and extend it until it intersects the reference sphere at point A. Line AS is then obtained by connecting point A and polar point S, and line AS intersects equatorial plane at point A'. As illustrated in Fig. 1(d), the spherical coordinate of point A can be expressed in terms of (r_A, α_A, φ_A),

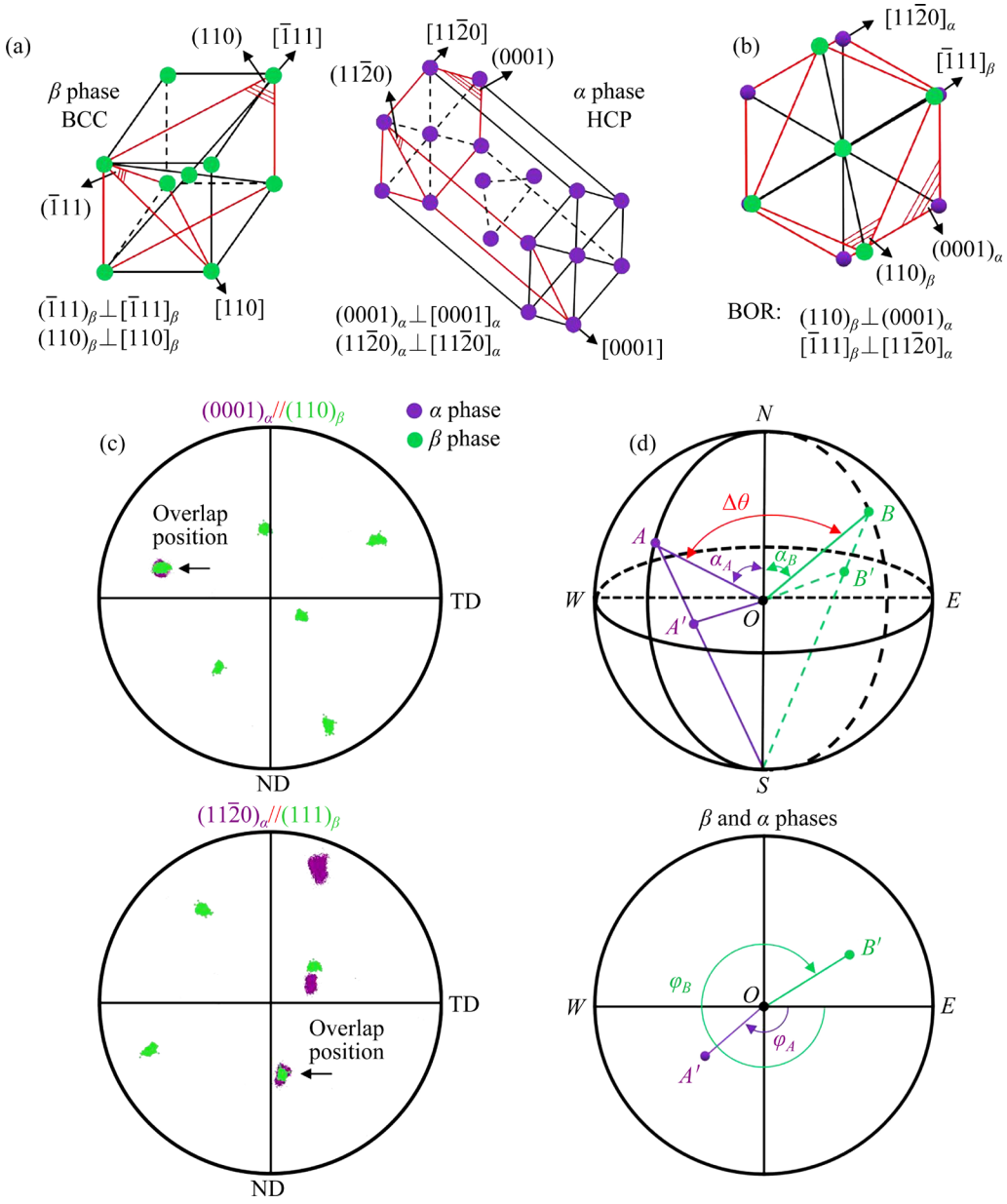

Fig. 1 (a, b) Schematic diagrams of ideal BOR; (c) BOR between α and β phases in titanium alloy; (d) Schematic diagrams of spherical center angle ($\Delta\theta$) between α and β phases

where r_A is defined as the radius of the sphere (r>0), α_A is defined as the angle between OA and sphere's axis NS ($0\leq\alpha_A\leq\pi/2$), φ_A is given as the angle between OA' and diameter line WE ($0\leq\varphi\leq2\pi$). Likewise, $(11\bar{2}0)_\alpha$, $(110)_\beta$ and $(111)_\beta$ pole stereographic projections can be acquired concerning their unit cells. For convenience, one plane of α phase and one plane of β phase are assumed to be located in the same spherical coordinate system, as shown in Fig. 1(d). The normals OA and OB form a spherical center angle $\Delta\theta$ ($0\leq\Delta\theta\leq2\pi$), which is also the angle between the two corresponding planes.

In spatial Cartesian coordinate system, the distance L between points A (x_A, y_A, z_A) and B (x_B, y_B, z_B) can be calculated by following equation:

$$L=\sqrt{(x_A-x_B)^2+(y_A-y_B)^2+(z_A-z_B)^2} \quad (1)$$

The spatial Cartesian coordinate system of points A (x_A, y_A, z_A) and B (x_B, y_B, z_B) and the spherical coordinate system of points A (r_A, α_A, φ_A) and B (r_B, α_B, φ_B) are related as follows:

$$\begin{cases} x_A=r_A\sin\alpha_A\sin\varphi_A \\ y_A=r_A\sin\alpha_A\cos\varphi_A \\ z_A=r_A\cos\alpha_A \end{cases} \quad 2(a)$$

$$\begin{cases} x_B = r_B \sin\alpha_B \sin\varphi_B \\ y_B = r_B \sin\alpha_B \cos\varphi_B \\ z_B = r_B \cos\alpha_B \end{cases} \quad (2b)$$

Then, the distance L between points A (x_A, y_A, z_A) and B (x_B, y_B, z_B) follows

$$L = \{r_A^2 + r_B^2 - 2r_A r_B[\cos\alpha_A \cos\alpha_B + \sin\alpha_A \sin\alpha_B \cos(\varphi_A - \varphi_B)]\}^{1/2} \quad (3)$$

Moreover, the L of segment AB can also be obtained from the law of cosines in triangle OAB:

$$L = \sqrt{r_A^2 + r_B^2 - 2r_A r_B \cos\Delta\theta} \quad (4)$$

Combining Eqs. (3) and (4), we have

$$\cos\Delta\theta = \cos\alpha_A \cos\alpha_B + \sin\alpha_A \sin\alpha_B \cos(\varphi_A - \varphi_B) \quad (5)$$

Thus, the spherical center angle ($\Delta\theta$) can be calculated as follows:

$$\Delta\theta = \arccos[\cos\alpha_A \cos\alpha_B + \sin\alpha_A \sin\alpha_B \cos(\varphi_A - \varphi_B)] \quad (6)$$

In HCP and BCC crystal structures, several nonparallel planes or directions with different indices are crystallographically equivalent. This means that several poles exist simultaneously in PFs, as shown in Fig. 1(c). Considering that there are m equivalent indices in one plane or direction of α phase and n equivalent indices in one plane or direction of β phase, the minimum value of the spherical center angle is the misorientation angle between planes or directions, then $\Delta\theta$ follows

$$\Delta\theta = \mathrm{Min}\{\arccos[\cos\alpha_i \cos\alpha_j + \sin\alpha_i \sin\alpha_j \cos(\varphi_i - \varphi_j)]\} \quad (i=1, \cdots, m, j=1, \cdots, n) \quad (7)$$

Supposing that we use Eq. (7) to calculate the angular deviations from the ideal BOR between α and β phases in titanium alloys, some special spatial relationships associated with the BOR should be highlighted. One unique feature of BCC crystal structure is that planes and directions with the same indices are perpendicular to one another. For example, $[\bar{1}11]_\beta$ direction is perpendicular to $(\bar{1}11)_\beta$ plane, and $[110]_\beta$ direction is perpendicular to $(110)_\beta$ plane. In HCP crystal structure, there is not always a perpendicular geometrical relationship between planes and directions with the same indices. However, it is easy to prove that $[11\bar{2}0]_\alpha$ direction is perpendicular to $(11\bar{2}0)_\alpha$ plane, and $[0001]_\alpha$ direction is perpendicular to $(0001)_\alpha$ plane, as shown in Fig. 1(a).

2.2 Experiment

In this study, cylindrical samples with d10 mm × 15 mm were cut from the alloy bars with nominal compositions of Ti−6Al−4V and Ti−6.5Al−2Zr−1Mo−1V for β annealing treatments. Samples of Ti−6Al−4V alloy were initially β-annealed at 1030 °C for 2 h, then cooled in a furnace to 750 °C at a controlled rate of ~0.25 °C/min and soaked for 2 h, and finally air-cooled to ambient temperature. Similarly, Ti−6.5Al−2Zr−1Mo−1V alloy samples were originally β-annealed at 1050 °C for 2 h, then cooled in a furnace to 750 °C at a controlled rate of ~0.3 °C/min and soaked for 2 h, and finally air-cooled to ambient temperature. All samples were coated with an antioxidant coating to prevent oxidation before β annealing treatments.

The optical microscopy (OM) and scanning electron microscopy (SEM) samples were ground with SiC papers to 2000# grit and polished by colloidal silica and then etched in Korll's reagent (3 vol.% HF + 6 vol.% HNO_3 + 91 vol.% H_2O). The transmission electron microscopy (TEM) samples were initially machined using the electrical discharge machine to achieve a thickness of 0.5 mm. Subsequently, mechanical polishing reduced their thickness to 20 μm, followed by punching to produce discs with a diameter of 3 mm. Finally, the discs underwent electropolishing using a twin-jet electro-polisher device. TEM observations were performed with an FEI/Thermo scientific Themis Z, at 300 kV. During high-angle annular dark-field scanning transmission electron microscopy (HAADF-STEM) observations, the electron beam was aligned parallel to $[011]_\beta // [0001]_\alpha$ and $[\bar{1}11]_\beta // [2\bar{1}\bar{1}0]_\alpha$ directions to observe the α/β interfaces from different directions.

The electron backscattering diffraction (EBSD) samples were electro-polished in an electrolyte solution of 6 vol.% perchloric acid, 64 vol.% methyl alcohol and 30 vol.% butanol for ~45 s with a voltage of 20 V at a temperature of −10 °C. The measurements were conducted using a JSM−7900F SEM equipped with an EDAX EBSD HIKARI XP. The EBSD scanning was performed at a step size of 0.2 μm. It is necessary to obtain α and φ angles when calculating spherical center angle $\Delta\theta$. The main steps are as follows. Firstly, we select a single point on the automated inverse pole figure (IPF) map using point model in highlighting toolbar, and

the software will record the orientation data for the point that we are interested in. Secondly, we right-click on the selected data point, and a new subset can be created for further analysis. Thirdly, we click the auto-PF function option in quick-gen toolbar. The software will generate a discrete PF for the new subset. From the auto-PF, α and φ angles of the point can be obtained. It should be noted that α and φ angles change relatively when projecting PFs by stereographic, equal area or equal angle, but this will not affect the final calculation results. In this study, all PFs in software were set to project by stereographic.

3 Results

Figures 2(a) and (b) show the OM images of Ti−6Al−4V and Ti−6.5Al−2Zr−1Mo−1V samples subjected to β annealing treatment, respectively. It was found by OM observations that the fully lamellar microstructures are obtained after β annealing treatment. The average sizes of β grains in Ti−6Al−4V and Ti−6.5Al−2Zr−1Mo−1V samples are ~650 and ~500 μm, respectively. In addition, the cooling rates from β phase field were precisely controlled to optimize the morphologies of α_{GB} phase and α colonies with low residual thermal stress. As shown in Figs. 2(a) and (b), continuous α_{GB} phase can be observed at the β grain boundaries, and one β grain usually consists of several α colonies with different orientations. Notably, the sizes of α colonies in Ti−6Al−4V and Ti−6.5Al−2Zr−1Mo−1V samples are 100−300 and 100−250 μm, respectively.

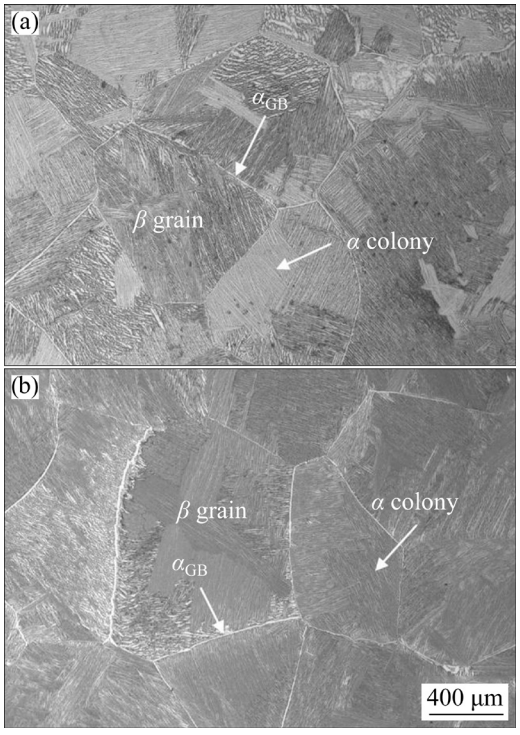

Fig. 2 OM images of Ti−6Al−4V (a) and Ti−6.5Al−2Zr−1Mo−1V (b) samples after β annealing treatment

Figures 3(a) and (g) display the magnified views of α colonies in Ti−6Al−4V and Ti−6.5Al−2Zr−1Mo−1V samples by SEM, respectively. It is found by SEM observations that the α colonies consist of alternating layers of α and retained β phases, with all α plates growing roughly parallel to each other. The average thickness of α plates for both samples is ~3 μm.

Figures 3(b) and (h) show the IPF maps of Ti−6Al−4V and Ti−6.5Al−2Zr−1Mo−1V samples at low magnification, respectively. It is worth noting that α plates in an α colony have the same color, indicating that they belong to a single crystallographic variant. Theoretically, a total of 12 α colony variants can occur during $\beta\rightarrow\alpha$ phase transformation. However, as illustrated in Figs. 3(b) and (h), the number of α colony variants in β grains is usually limited due to variant selection [18,19]. In adjacent β grains, α_{GB} phase has the same color as the nearest α colony in one of the grains, indicating that the α_{GB} phase and the nearest α colony share the same crystallographic orientation. A possible reason for this observation may involve the fact that α_{GB} phase usually precipitates preferentially and can serve as a preferred site for the nucleation of α colony during $\beta\rightarrow\alpha$ phase transformation [1,16].

As shown in Figs. 3(c) and (i), a typical α colony was selected from Figs. 3(b) and (h) to calculate the angular deviations. As illustrated in Figs. S1(a) and (b) in Supplementary Materials (SM), one pole in $(0001)_\alpha$ and one pole in $(110)_\beta$ PFs show the same positions (as indicated by black arrows), as well as one pole in $(11\bar{2}0)_\alpha$ and one pole in $(111)_\beta$ PFs, indicating that α and β phases in selected α colonies obey the BOR. Furthermore, all poles in PFs show a dispersed distribution, suggesting a deviation in crystallographic orientation. As illustrated in Figs. 3(c) and (i), we randomly selected 100 points at 50 positions in α colonies of Ti−6Al−4V and Ti−6.5Al−2Zr−1Mo−1V samples to calculate the angular deviations, respectively. All orientation data for α and β phases

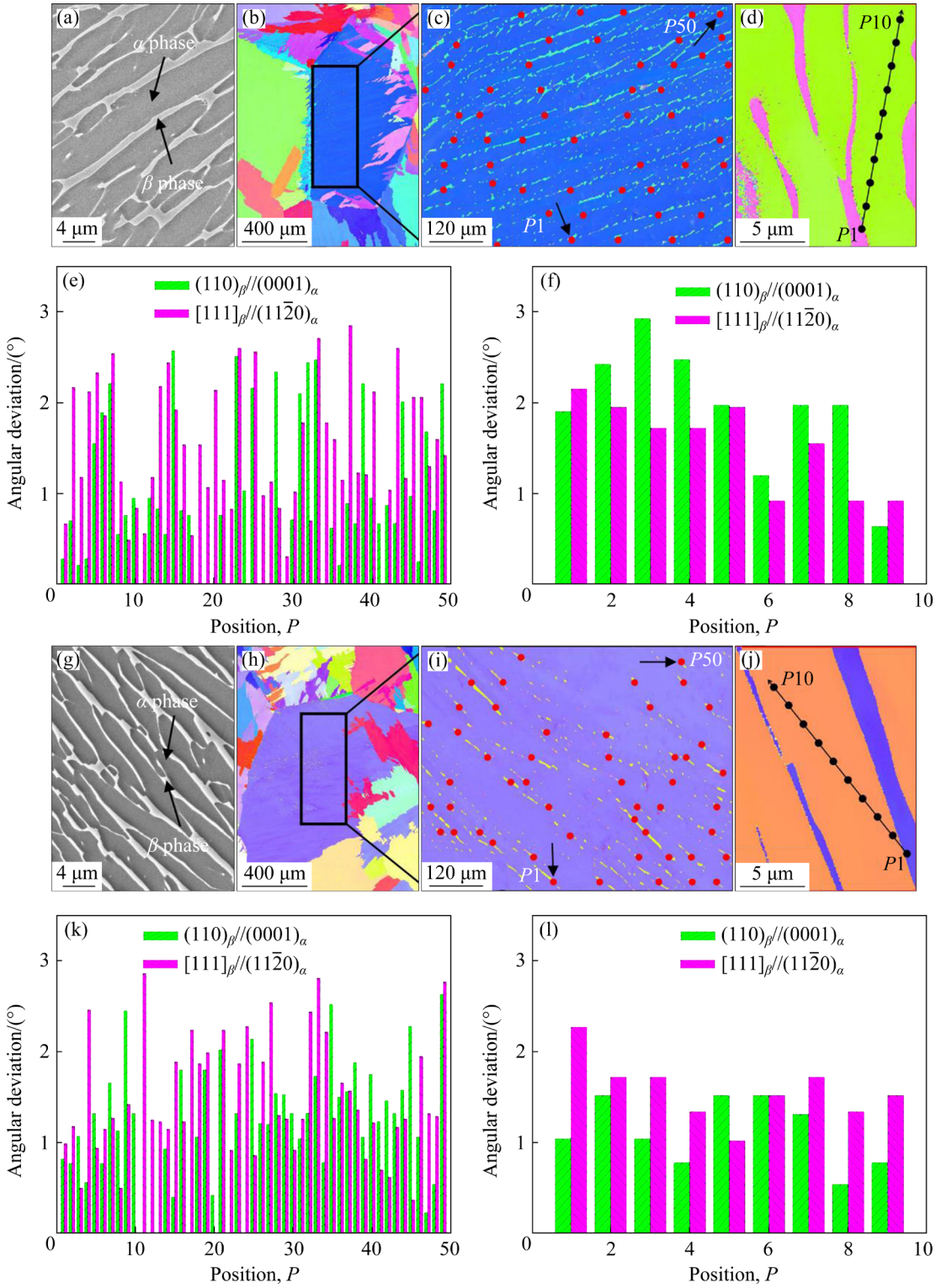

Fig. 3 SEM images (a, g), IPF maps (b–d, h–j), and angular deviation values (e, f, k, l) of Ti−6Al−4V (a–f) and Ti−6.5Al−2Zr−1Mo−1V (g–l) samples

were obtained near the α/β interfaces. The results are presented in Tables S1 and S2 in SM, respectively. The corresponding calculated angular deviation values of the two samples are shown in Figs. 3(e) and (k), respectively. In Ti−6Al−4V sample, the angular deviation values between $(0001)_\alpha$ and $(110)_\beta$ planes range from 0° to 2.57°, and the values between $[11\bar{2}0]_\alpha$ and $[111]_\beta$ directions range from 0° to 2.85°. In the case of Ti−6.5Al−2Zr−1Mo−1V sample, the angular

deviation values between $(0001)_\alpha$ and $(110)_\beta$ planes range from 0° to 2.63°, and the values between $[11\bar{2}0]_\alpha$ and $[111]_\beta$ directions range from 0° to 2.86°. Referring to the calculation results, it is clear that no perfect BOR exists between α and β phases, and all angular deviation values are consistently less than 3.0°.

Figures 3(d) and (j) show the magnified IPF maps of α colonies in the two samples, respectively. The corresponding PFs shown in Figs. S1(c) and (d) in SM exhibit analogous results to those in Figs. S1(a) and (b) in SM. We selected 10 points along the line segment to calculate the angular deviations to investigate the position chosen on the results. As illustrated in Figs. 3(d) and (j), the position of point 1 lies in the β phase and the remaining points are located in the α phase. The calculation results for the two samples are presented in Tables S3 and S4 in SM, respectively. As shown in Figs. 3(f) and (l), the results are in agreement with our previous findings, i.e., the angular deviation values $\Delta\theta$ for all results are less than 3.0°. This implies no significant change in the calculation results of the two samples when the position moves from point 2 to point 10.

Combining the results shown in Tables S1−S4 in SM, a certain degree of angular deviation from the ideal BOR is always found in α colonies of the two samples, and the tolerance angle value appears to be 3.0°.

4 Discussion

In metals with HCP crystal structures, such as titanium and zirconium, the BOR law will be followed during $\beta\rightarrow\alpha$ phase transformation since it leads to the lowest low-energy interfaces between the two phases [1,3]. According to BURGERS' finding [3], the ideal BOR law is followed between the two phases in the case of shear phase transformation. However, our results show that there is no evidence to support the perfect BOR between the two phases during diffusion-controlled phase transformation, and the angular deviation values $\Delta\theta$ are consistently less than 3.0°. In this section, we focus on the crystallographic orientations and interface features in α colonies via EBSD and HAADF-STEM observations to investigate the causes of the angular deviations.

4.1 Misorientation distribution in single phase

Figures 4(a) and (g) display the grain boundary (GB) images of the two samples. In GB images, the misorientation angles of boundaries from 2.0° to 15.0° and those larger than 15.0° are illustrated in red and blue colors, respectively. It is found that all α/β interfaces are marked in blue color and are therefore ascribed as high-angle grain boundaries (HAGBs). As shown by the black arrows in GB images, the misorientations within α and β phases are less than 2.0°, indicating that no sub-grain boundaries are formed in grains.

Figures 4(b) and (h) show the kernel average misorientation (KAM) images of the two samples. KAM represents the local geometric necessary dislocation (GND) density by calculating the GND quantitatively in microstructure, with higher values indicating higher defect density [24]. Referring to the KAM observation results, it can be found that the highest dislocation densities are mainly located at α/β interfaces. This implies that dislocations developed sequentially and formed with equal amounts of shear strain at α/β interfaces during $\beta\rightarrow\alpha$ phase transformation [25−28].

Figures 4(c) and (i) show the line paths in IPF images to measure the misorientations in α colonies. Specifically, Lines 1 and 4 are the paths to measure the misorientations that cross α and β phases in Ti−6Al−4V and Ti−6.5Al−2Zr−1Mo−1V samples, respectively. Lines 2 and 5 are the paths for measuring the misorientations in α phase, and lines 3 and 6 are the paths to determine the misorientations in β phase. Figures 4(d) and (j) display the point-to-origin misorientation curves of the two phases in Ti−6Al−4V and Ti−6.5Al−2Zr−1Mo−1V samples, respectively. It has been demonstrated that the α/β interfaces in α colonies belong to HAGBs with a misorientation of ~45.0°, and the misorientations within a single phase show an undulating feature. The point-to-origin misorientation curves of the single phase for the two samples are shown in Figs. 4(e, f) and (k, l). In Ti−6Al−4V sample, as the distance changes, the misorientation values within α phase remain relatively constant, while the misorientation values of β phase show a slightly increasing trend. In the case of Ti−6.5Al−2Zr−1Mo−1V sample, the misorientation values of both phases show an increasing trend initially, followed by a decreasing trend as the distance changes. Although misorientation

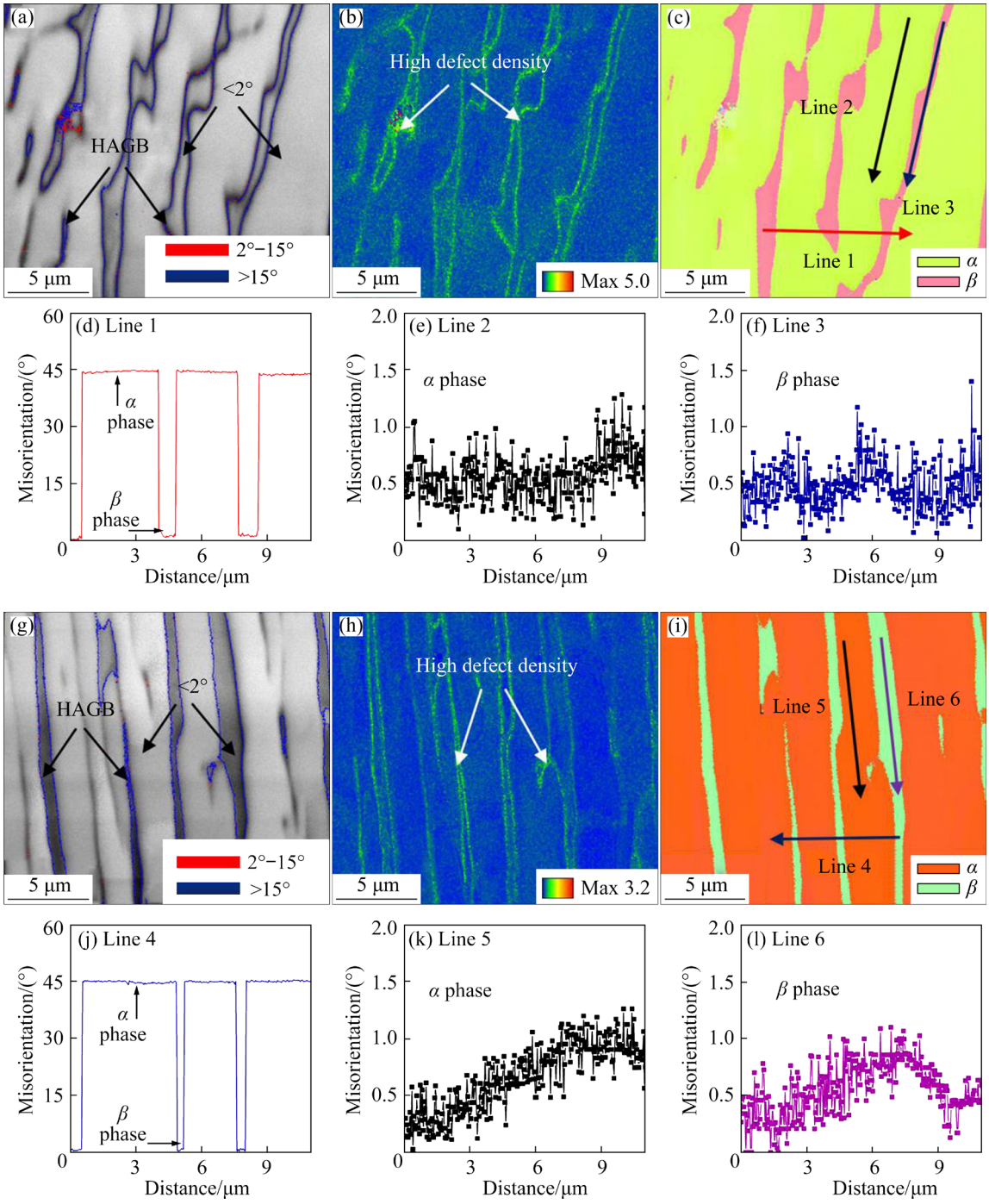

Fig. 4 GB (a, g), KAM (b, h), IPF (c, i) images and point-to-origin misorientation curves (d−f, j−l) of Ti−6Al−4V (a−f) and Ti−6.5Al−2Zr−1Mo−1V (g−l) samples

curves of the single phase show fluctuating features, the values of misorientations in the two samples are below 1.5°.

Figures 5(a) and (f) present low magnification HAADF-STEM images of α phase in Ti−6Al−4V and Ti−6.5Al−2Zr−1Mo−1V samples, respectively. The incident directions of electron beam are labeled as $[2\bar{1}\bar{1}0]_\alpha$ and $[0001]_\alpha$, respectively. The corresponding selected area electron diffraction (SAED) images are presented in the upper right corner of the HAADF-STEM images, which help to determine the orientations of atomic planes. In HAADF mode, the intensity peaks (bright spots) appear at the positions of atomic columns. The intensity is roughly proportional to Z^2, where Z represents the average atomic number of each

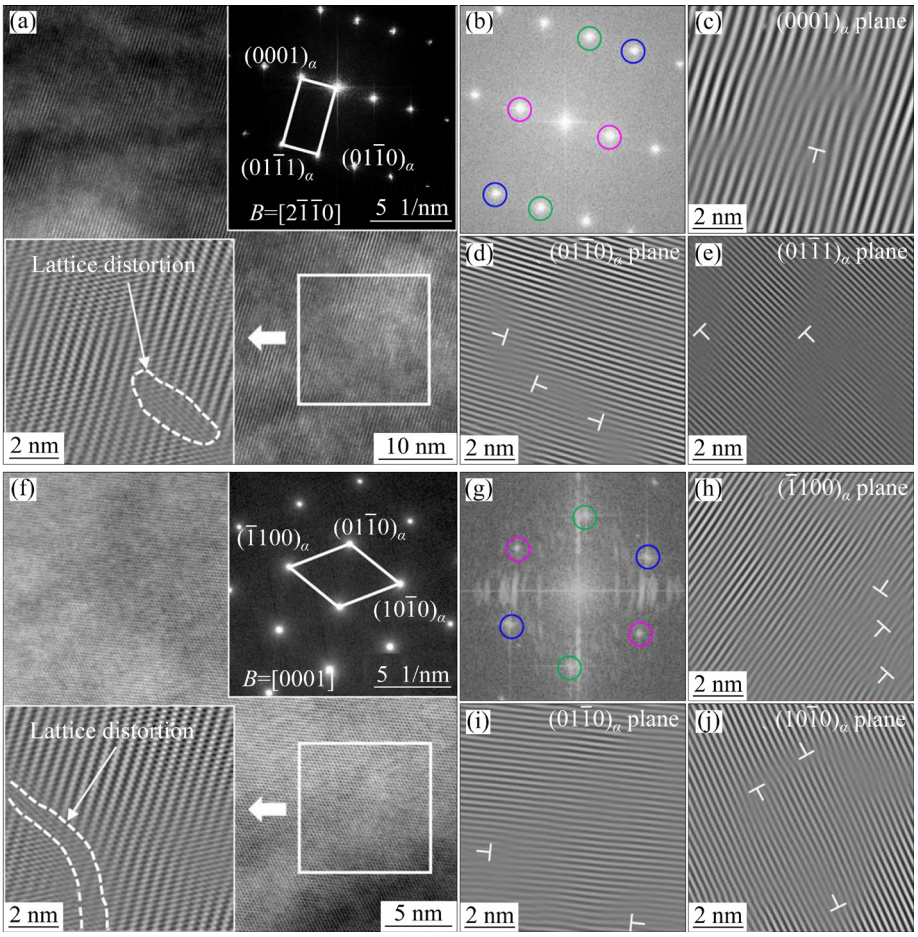

Fig. 5 HAADF-STEM (a, f), FFT (b, g) and IFFT (c−e, h−j) images of α phase in Ti−6Al−4V (a−e) and Ti−6.5Al−2Zr−1Mo−1V (f−j) samples

column [29]. Therefore, the atomic arrangements and element distribution information can be further analyzed. As shown in Figs. 5(a) and (f), two regions (white-solid rectangles in HADDF-STEM images) were selected to perform fast Fourier transform (FFT) and the corresponding FFT images are shown in Figs. 5(b) and (g), respectively. It is worth noting that the real-time diffraction spots in FFT images are in accordance with the SAED spots, indicating that all the chosen regions belong to α phase. In Ti−6Al−4V sample, the features of $(0001)_\alpha$, $(01\bar{1}0)_\alpha$ and $(01\bar{1}1)_\alpha$ planes are obtained using inverse Fourier fast transform (IFFT), as shown in Figs. 5(c−e), respectively. Notably, many edge dislocations and resulting significant distortions are observed in all planes, with greater distortions around edge dislocations. In addition, the lowest index plane $(0001)_\alpha$ exhibits a severer distortion. Figures 5(h−j) show IFFT images of $(\bar{1}100)_\alpha$, $(01\bar{1}0)_\alpha$ and $(10\bar{1}0)_\alpha$ planes in Ti−6.5Al−2Zr−1Mo−1V sample, respectively. The edge dislocations and lattice distortions are also found in three low-index planes, and the degree of distortion is comparable.

It has been well recognized that the dislocations in microstructure affect the atomic arrangements, resulting in significant distortion of atomic columns and differences in atomic spacing. This phenomenon is particularly apparent in IFFT pattern, as shown by the white arrows in the bottom left corner of Figs. 5(a) and (f). As a matter of fact, dislocations inevitably occur in real polycrystalline materials. In practice, titanium alloy undergoes multiple phase transformations from liquid phase to β phase and then to α phase as the temperature decreases, forming a titanium ingot. Subsequently, titanium ingot is usually subjected to cycles of hot deformation and heat treatments. As a result, the dislocations are commonly formed during solidification of crystalline solids, cold/hot plastic deformation, vacancy condensation, and atomic mismatch in solid solutions [30]. The origination,

multiplication, and extinction of dislocations occur simultaneously in these processes. Upon continuous cooling from a single β phase field, α phase tends to nucleate and precipitate preferentially in defective regions such as β grain boundaries and dislocations. In this case, dislocations are generated due to thermal stresses and chemical micro-segregation. Thus, the reasons for accumulated misorientations within α and β phases (usually less than 1.5°) can be well illustrated by the following explanations. The local variations of misorientations are strongly correlated with the defects in real crystal materials. The dislocations that occur during phase transformation disrupt crystal perfection and lead to a slight change in crystal growth direction. This not only influences the local atomic arrangements but also induces lattice distortions, resulting in minor changes in crystallographic orientations of the two phases.

4.2 Structure characteristics of α/β interfaces

Figures 6(a−e) show the TEM images of α/β interfaces viewed along $[011]_\beta//[0001]_\alpha$ direction in Ti−6Al−4V sample. As shown in the bright field (BF) TEM image of Fig. 6(a), the α/β interfaces appear relatively flat in this view. Additionally, no dislocation networks or walls are observed within the two phases or near α/β interfaces. The HAADF-STEM image of α/β interfaces and the corresponding SAED pattern are presented in Figs. 6(b) and (c), respectively. As illustrated in Fig. 6(b), the broad surface of α/β interfaces can be described as structure ledges, also known as terrace ridges. Previous studies showed that these ledges were incoherent and, therefore, mobile, which determined the mobility of α/β interfaces and the thickening rate of α plates; in contrast, the terraces were coherent and immobile [26,31]. The HAADF-STEM image shown in Fig. 6(b) clearly indicates that the terraces are oriented perpendicularly to $[11\bar{2}0]_\alpha//[\bar{1}11]_\beta$ direction, and the ledges align with $(01\bar{1})_\beta$ plane, which has an angle of ~6.0° with $(01\bar{1}0)_\alpha$ plane. The height of the ledges is typically several times $(21\bar{1})_\beta$ plane spacing. This result is consistent with previous research findings [31,32]. In addition, as shown in Fig. 6(b), the lattice distortions become obvious near α/β interfaces, and the region of distortions near α/β interfaces in α phase is approximately ~1.5 nm. Figures 6(d) and (e) show the IFFT images of $(\bar{1}100)_\alpha$ and $(200)_\beta$ planes, respectively. It is clearly seen that there are many edge dislocations in both planes, and the lattice dislocations in $(\bar{1}100)_\alpha$ plane are mainly concentrated near β region while in $(200)_\beta$ lane primarily appear near α region.

Figures 6(f–j) show the TEM images of α/β interfaces viewed along $[\bar{1}11]_\beta//[2\bar{1}\bar{1}0]_\alpha$ direction in Ti−6.5Al−2Zr−1Mo−1V sample. As illustrated in the BF image of Fig. 6(f), the results are analogous to those in Ti−6Al−4V sample, and no dislocation networks or walls are observed within the two phases or near α/β interfaces. Figures 6(g) and (h) display the HAADF-STEM image of α/β interfaces and corresponding SAED pattern, respectively. As shown in Fig. 6(g), the matching pattern of atomic columns along α/β interfaces for the two phases is almost perfect. This feature may reveal the nature of the lattice invariant deformation (LID) ideal model lying in the terrace planes. The α/β interfaces shown in Fig. 6(g) could be identified using real-time FFT diffraction spots, and non-uniformly mixed atomic columns can be observed near the α/β interfaces. Herein, the green dots represent the atomic columns of β phase, and the red dots denote the atomic columns of α phase, which are then overlaid with the atomic columns in the HAADF-STEM image, respectively. As shown in Fig. 6(g), the atomic columns of the two phases match one-to-one between $(0001)_\alpha$ plane and $(101)_\beta$ plane at α/β interfaces, and the broad face of α/β interfaces consists of atomic structure ledges, and their terraces parallel to $(0001)_\alpha//(101)_\beta$ and ledges parallel to $(01\bar{1}\bar{1})_\alpha$ plane, which has an angle of ~3.5° with $(0\bar{1}1)_\beta$ plane. By observing the IFFT images of $(101)_\beta$ and $(0001)_\alpha$ planes shown in Figs. 6(i) and (j), many edge dislocations and resulting lattice distortions can be found in both planes. Additionally, the lattice distortions in $(0001)_\alpha$ plane are more pronounced, especially at α/β interfaces, where the degree of lattice distortions becomes much severer because of more edge dislocations.

As mentioned in previous study [26], the macroscopic broad face of α/β interfaces viewed along $[011]_\beta//[0001]_\alpha$ direction had an irrational habit plane close to $\{111\}_\beta$, such as $(\bar{1}\bar{1}\bar{1}\bar{1}13)_\beta$ plane. This habit plane resulted from the uniform arrangement of structure ledges that stepped down

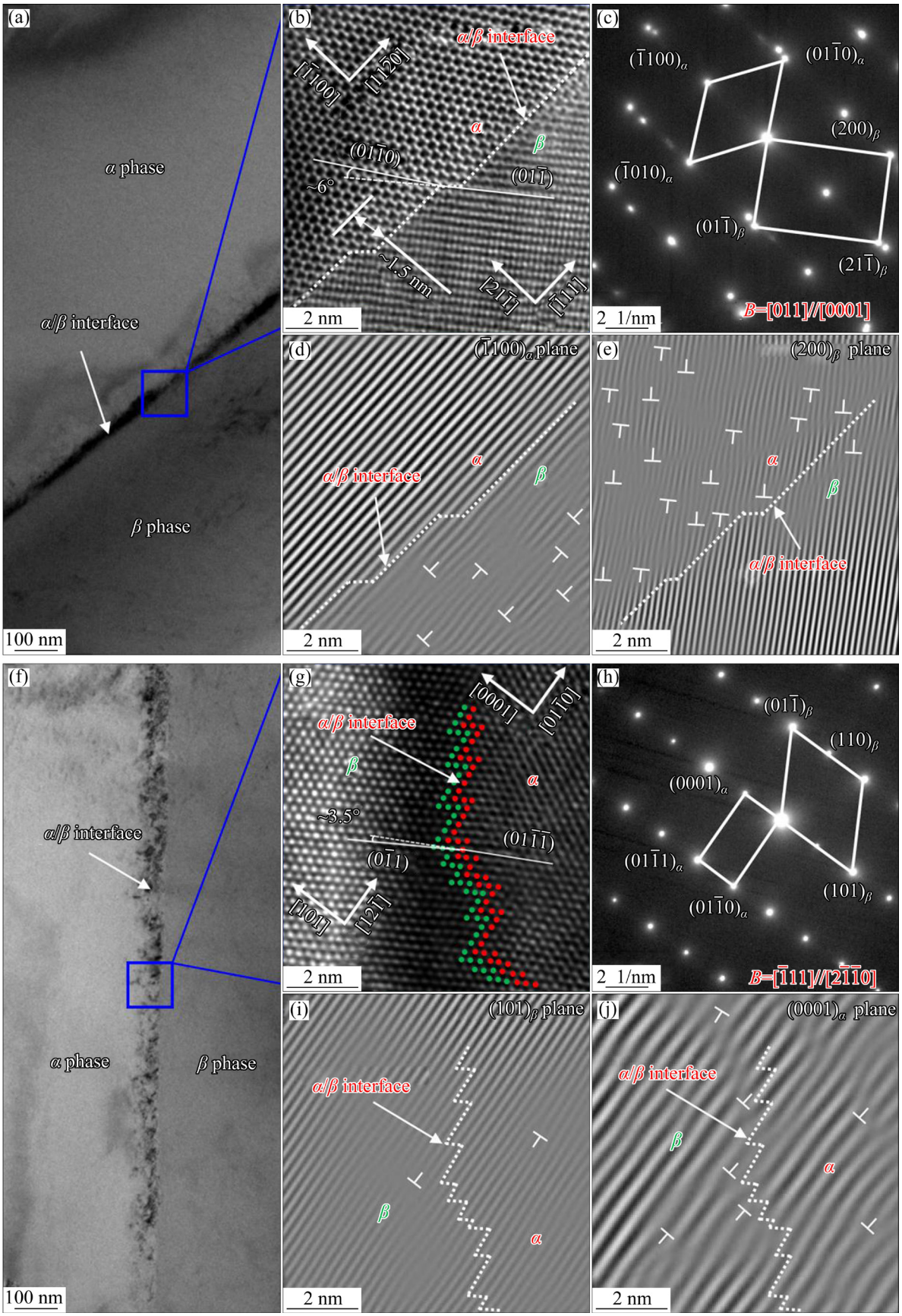

Fig. 6 BF TEM (a, f), HAADF-STEM (b, g), SAED (c, h) and IFFT (d, e, i, j) images of α/β interfaces in Ti−6Al−4V (a−e) and Ti−6.5Al−2Zr−1Mo−1V (f−j) samples

along the lattice invariant ling (approximately $[\bar{3}35]_\beta$) with terraces and minimized the elastic strain energy. As a result, ⟨*a*⟩, ⟨*c*⟩, and ⟨*c*+*a*⟩ types of mismatch dislocations existed along the lattice invariant line. For example, in *β*-solutionized and aged Ti−6.6Cr alloy, and annealed Ti−5Al−2.5Sn−0.05Fe alloys, *c*-type dislocations ($b=c_\alpha=[0001]_\alpha$) were observed on the habit planes of *α*/*β* interfaces [25,26]. Meanwhile, *a*-type dislocations ($b=a_\alpha=1/3[11\bar{2}0]_\alpha$) and (*c*+*a*)-type dislocations ($b=c_\alpha+a_\alpha=1/6[2\bar{1}\bar{1}3]_\alpha$) were found on the habit planes of *α*/*β* interfaces in Ti−Cr alloys [27,28]. In the present study, the broad face of *α*/*β* interfaces viewed along two different directions in HAADF-STEM images shows the atomic-scale terrace-ledge characteristics, with many dislocations and severe lattice distortions near *α*/*β* interfaces. The HADDF-STEM observation results are in good agreement with the KAM images shown in Figs. 4(b) and (h), further indicating that the maximum dislocation density is located near the *α*/*β* interfaces. The results of this study also confirm that lattice distortions are correlated closely with dislocations and *α*/*β* interfaces in microstructure.

The lattice distortions caused by dislocations are also associated with solute elements. Figure S2 in SM shows the energy dispersive spectroscopy (EDS) line profiles and element distribution of *α* and *β* phases in both samples. In Ti−6Al−4V sample, *β* phase is enriched with V element and *α* phase contains Al-rich element, as shown in Figs. S2(a) and (c) in SM. In the case of Ti−6.5Al−2Zr−1Mo−1V sample, Mo and V elements are enriched in *β* phase, Al element is enriched in *α* phase, and Zr is homogeneously distributed in both phases, as illustrated in Figs. S2(b) and (c) in SM. It is worth noting that although both Mo and V elements are enriched in *β* phase, the location of the maximum concentration near *α*/*β* interfaces is different due to varying diffusion rates. In fact, the precipitation of *α* phase from *β* parent phase can be regarded as the *α*/*β* interfaces gradually entering *β* phase at a certain velocity. This process is typically represented using the classical terrace-ledge-kink model [31,33], where the terraces are coherent and immobile, and simultaneously, the ledges are considered incoherent and movable. Thus, the movement of the ledges is controlled by long-range diffusion to change the micro-chemical composition of *α* and *β* phases at *α*/*β* interfaces.

During *β*→*α* phase transformation, the diffusion distances of elements strongly depend on temperature and local micro-chemical composition. For example, *α* phase has very limited solubility for V and Mo elements, so they will accumulate from *α* phase to *α*/*β* interfaces. Meanwhile, Al element is also enriched from *β* phase to *α*/*β* interfaces. Because the cooling rate is slow enough at elevated temperatures, the alloy elements have high diffusion rates, making it easy to reach the thermodynamic equilibrium of *α* phase at *α*/*β* interfaces and precipitate new *α* phase. After air cooling from 750 °C, the kinetic of *β*→*α* phase transformation is suppressed because the diffusion distances of alloy elements would be significantly reduced with higher cooling rate. As a result, there is still an excessive atomic enrichment at *α*/*β* interfaces, leading to lattice distortions accommodated by dislocations of *α*/*β* interfaces.

4.3 Influence of *α*/*β* interfaces on misorientations

As shown in Figs. 6(b) and (g), a minor angular deviation exists at the ledge contact between the atomic planes of *α* and *β* phases. In fact, lattice mismatch usually occurs at *α*/*β* interface due to different crystal structures and lattice constants. According to the phenomenological theory of martensite crystallography (PTMC), the calculated ideal angular deviation between $[11\bar{2}0]_\alpha$ and $[111]_\beta$ directions is 0.5° in titanium alloy [34]. However, our results show that most values are larger than 0.5°. This implies that other influential factors at *α*/*β* interfaces cannot be ignored in real crystals. As a matter of fact, *α*/*β* interface belongs to semi-coherent type, and this type of interface provides the lowest total transformation shape strain and corresponding strain energy during *β*→*α* phase transformation [3,26]. Since *α*/*β* interfaces form a transformation region between the two neighboring phases, the lattice mismatch in those regions causes local structure disorder and an excess energy configuration. We further found that *α*/*β* interfaces contain interface defects, including dislocations and structure ledges. These defects can not only accommodate lattice mismatch between the two different phases but also influence local arrangement patterns of atoms, leading to a slight change in crystallographic orientations.

In this study, we calculated the angular deviation values $\Delta\theta$ of *α* and *β* phases with respect

to the ideal BOR in α colonies of Ti−6Al−4V and Ti−6.5Al−2Zr−1Mo−1V alloys. In combination with the results, a tolerance angle ($\Delta\theta_T$) of 3° exists in α colonies for the two alloys. In addition, the two samples show similar results of misorientations under β annealing treatments, suggesting that the tolerance angle appears to be independent of the chemical composition of alloys. Further studies show that misorientations within a single phase are less than 1.5°. The HAADF-STEM results reveal that many dislocations and severe lattice distortions appear near α/β interfaces, thus influencing crystallographic orientations. Although the angular deviations caused by α/β interfaces have not been quantified in this study, it is reasonable to infer that α/β interfaces cause slight angular deviations between the two phases because of lattice mismatch, dislocation, and element rejection during $\beta\rightarrow\alpha$ transformation.

It should be noted that the tolerance angle $\Delta\theta_T$ is an important parameter in studying crystallographic evolutions of α colonies during hot working. Lacking a widely accepted consensus on the tolerance angle is likely a significant factor in the controversial results discussed in the introduction. Furthermore, the BOR variations and morphology evolutions for both phases are correlated closely with hot working. Specifically, the ORs between the two phases may change following the order of BOR→non-BOR→BOR as the ingots of titanium alloys undergo hot deformation caused by heat treatment. This calculation model can be used to quantify the effects of hot working parameters on BOR variations.

5 Conclusions

(1) A model was introduced to calculate the angular deviations from the ideal BOR. The underlying influence factors in microstructures were studied by OM, SEM, EBSD and HAADF-STEM observations.

(2) The α/β interfaces in Ti−6Al−4V and Ti−6.5Al−2Zr−1Mo−1V alloys show atomic-scale terrace−ledge structure when viewed from two different directions. At the contact positions of the ledges, minor angular deviations occur due to lattice mismatch between the atoms of α and β phases.

(3) The regions within α and β phases and near α/β interfaces exhibit dislocations and resulting lattice distortions. The misorientations in α and β phases are attributed to lattice distortions by dislocations, which affect the local atomic arrangements in microstructures.

(4) Considering the α/β interfaces and defects in polycrystalline titanium alloys, a tolerance angle, such as 3.0° in this study, could be used to determine whether α and β phases obey the BOR law.

CRediT authorship contribution statement

Ming-bing LI: Conceptualization, Investigation, Writing − Original draft, Writing − Review and editing; **Kai WANG:** Investigation, Data curation, Writing − Review and editing; **Bin WANG**, **Chao LV** and **Xin-nan WANG:** Investigation; **Xing LI:** Investigation, Data curation; **Zhi-shou ZHU:** Resourses, Project administration, Funding acquisition, Supervision; **Hui-long HOU:** Funding acquisition, Supervision; **Xin-qing ZHAO:** Resourses, Project administration, Funding acquisition, Supervision.

Declaration of competing interest

The authors declare that they have no known competing financial interests or personal relationships that could have appeared to influence the work reported in this paper.

Acknowledgments

This work was supported by the National Natural Science Foundation of China (Nos. 51971009, 12002013, 51831006), and the Natural Science Foundation of Zhejiang Province, China (No. LZ23E010004).

Supplementary Materials

Supplementary Materials in this paper can be found at: http://tnmsc.csu.edu.cn/download/08-p2830-2024-0103-Supplementary_Materials.pdf.

References

[1] LÜTJERING G, WILLIAMS J C. Titanium [M]. 2nd ed. New York: Springer, 2007.

[2] HUANG Liang, LI Chang-min, LI Cheng-lin, HUI Song-xiao, YU Yang, ZHAO Ming-jie, GUO Shi-qi, LI Jian-jun. Research progress on microstructure evolution and hot processing maps of high strength β titanium alloys during hot deformation [J]. Transactions of Nonferrous Metals Society of China, 2022, 32: 3835−3859.

[3] BURGERS W G. On the process of transition of the cubic-body-centered modification into the hexagonal-close-packed modification of zirconium [J]. Physica, 1934, 1: 561−586.

[4] WANG Duo-duo, FAN Qun-bo, YANG Lin, GONG Hai-chao, YUAN Jing-jiu, CHEN Kai, ZHU Xin-jie, CHENG Xing-wang, ZHOU Zhi-ming. Effects of rolling reduction on Burgers orientation relationship and slip behavior of a Ti−5.5Mo−7.2Al−4.5Zr−2.6Sn−2.1Cr alloy [J]. Journal of Materials Research and Technology, 2021, 15: 3099−3109.

[5] SOUVIK S, SHIBAYAN R. Novel insights on the grain boundary α phase microstructure formation and orientation development in Ti−6Al−4V alloy [J]. Journal of Alloys and Compounds, 2023, 968: 172265.

[6] BHATTACHARYYA D, VISWANATHAN G B, FRASER H L. Crystallographic and morphological relationships between β phase and the Widmanstätten and allotriomorphic α phase at special β grain boundaries in an α/β titanium alloy [J]. Acta Materialia, 2007, 55: 6765−6778.

[7] LU S L, TODARO C J, SUN Y Y, SONG T, BRANDT M, QIAN M. Variant selection in additively manufactured alpha-beta titanium alloys [J]. Journal of Materials Science & Technology, 2022, 113: 14−21.

[8] ZHANG Yu, XIN Ren-long, GUO Bao-qi, WANG Ke, LIU Qing. Influence of alternate grain boundary α on the development of Widmanstätten microstructure in TC21 Ti alloy [J]. Materials Characterization, 2021, 177: 111162.

[9] GAO Peng-fei, FU Ming-wang, ZHAN Mei, LEI Zhen-ni, LI Yan-xi. Deformation behavior and microstructure evolution of titanium alloys with lamellar microstructure in hot working process: A review [J]. Journal of Materials Science & Technology, 2020, 39: 56−73.

[10] MIRONOV S, MURZINOVA M, ZHEREBTSOV S, SALISHCHEV G A, SEMIATIN S L. Microstructure evolution during warm working of Ti−6Al−4V with a colony-α microstructure [J]. Acta Materialia, 2009, 57: 2470−2481.

[11] GEY N, BOCHER P, GERMAIN L, HUMBERT M. Texture and microtexture variations in a near-α titanium forged disk of bimodal microstructure [J]. Acta Materialia, 2012, 60: 2647−2655.

[12] ZHAO Z B, WANG Q J, LIU J R, YANG R. Effect of heat treatment on the crystallographic orientation evolution in a near-α titanium alloy Ti60 [J]. Acta Materialia, 2017, 131: 305−314.

[13] ZHOU Yu, WANG Ke, XIN Ren-long, LIU Qing. Effect of special primary α grain on variant selection of secondary α phase in a near-α titanium alloy [J]. Materials Letters, 2020, 271: 127766.

[14] LÜTJERING G. Influence of processing on microstructure and mechanical properties of (α+β) titanium alloys [J]. Materials Science and Engineering: A, 1998, 243: 32−45.

[15] PRITHIV T S, ZACHARY K, LI Dian, SHI Rong-pei, ZHENG Yu-feng, FRASER H L, GAULT B, ANTONOV S. Grain boundary segregation and its implications regarding the formation of the grain boundary α phase in the metastable β-titanium Ti−5Al−5Mo−5V−3Cr alloy [J]. Scripta Materialia, 2022, 207: 114320.

[16] SHI R, DIXIT V, FRASER H L, WANG Y. Variant selection of grain boundary α by special prior β grain boundaries in titanium alloys [J]. Acta Materialia, 2014, 75: 156−166.

[17] DASH B, JANGID R, KONERU S R, PILCHAK A, BANERJEE D. The formation of α at triple junctions of parent β phase in titanium alloys [J]. Philosophical Magazine, 2019, 99: 956−970.

[18] STANFORD N, BATE P S. Crystallographic variant selection in Ti−6Al−4V [J]. Acta Materialia, 2004, 52: 5215−5224.

[19] GEY N, HUMBERT M. Characterization of the variant selection occurring during the $\alpha\rightarrow\beta\rightarrow\alpha$ phase transformations of a cold rolled titanium sheet [J]. Acta Materialia, 2002, 50: 277−287.

[20] QIU Dong, ZHANG Ming-xing, KELLY P M, FURUHARA T. Crystallography of surface precipitates associated with shape change in a Ti−5.26wt.%Cr alloy [J]. Acta Materialia, 2013, 61: 7624−7638.

[21] LIU Tao, GERMAIN L, TEIXEIRA J, AEBY-GAUTIER E, GEY N. Hierarchical criteria to promote fast and selective α_{GB} precipitation at β grain boundaries in β-metastable Ti-alloys [J]. Acta Materialia, 2017, 141: 97−108.

[22] ZHANG Yu, XIN Ren-long, WANG Ke, LIU Qing. Variant selection of α precipitates formed at β triple junctions in titanium alloy [J]. Materials Characterization, 2022, 189: 111975.

[23] FU Jun-wei. A general approach to determine texture patterns using pole figure [J]. Journal of Materials Research and Technology, 2021, 14: 1284−1291.

[24] WANG Ke, WU Ming-yu, YAN Zhi-bing, LI Dong-rong, XIN Ren-long, LIU Qing. Microstructure evolution and static recrystallization during hot rolling and annealing of an equiaxed-structure TC21 titanium alloy [J]. Journal of Alloys and Compounds, 2018, 752: 14−22.

[25] FURUHARA T, HOWE J M, AARONSON H I. Interphase boundary structures of intragranular proeutectoid α plates in a hypoeutectoid TiCr alloy [J]. Acta Metallurgica Materialia, 1991, 39: 2873−2886.

[26] FURUARA T, OGAWA T, MAKI T. Atomic structure of interphase boundary of an α precipitate plate in a β Ti−Cr alloy [J]. Philosophical Magazine Letters, 1995, 72: 175−183.

[27] SARATH KUMAR MENON E, AARONSON H I. Interfacial structure of Widmanstatten plates in a Ti−Cr alloy [J]. Acta Metallurgica Materialia, 1986, 34: 1975−1981.

[28] YE F, ZHANG W Z, QIU D. A TEM study of the habit plane structure of intragranular proeutectoid α precipitates in a Ti−7.26wt.%Cr alloy [J]. Acta Materialia, 2004, 52: 2449−2460.

[29] PENNYCOOK S J, NELLIST P D. Scanning transmission electron microscopy imaging and analysis [M]. New York: Springer, 2002.

[30] SMITH W, HASHEMI J. Foundations of materials science and engineering [M]. 5th ed. Boston: McGraw Hill, 2009.

[31] ZHENG Yu-feng, WILLIAMS R E A, VISWANATHAN G B, CLARK W A T, FRASER H L. Determination of the structure of $\alpha-\beta$ interfaces in metastable β-Ti alloys [J]. Acta Materialia, 2018, 150: 25−39.

[32] ACKERMAN A K, VORONTSOV V A, BANTOUNAS I, ZHENG Yu-feng, CHANG Yan-hong, MCAULIFFE T,

CLARK W A, FRASER H L, GAULT B, RUGG D, DYE D. Interface characteristics in an α+β titanium alloy [J]. Physical Review Materials, 2020, 4: 013602.

[33] DAHMEN U. Surface relief and the mechanism of a phase transformation [J]. Scripta Metallurgica, 1987, 21: 1029−1034.

[34] POND R C, CELOTTO S, HIRTH J P. A comparison of the phenomenological theory of martensitic transformations with a model based on interfacial defects [J]. Acta Materialia, 2003, 51: 5385−5398.

钛合金在 $\beta\rightarrow\alpha$ 相变过程中 Burgers 位相关系的角度偏差及影响因素

李明兵[1,2]，王 凯[1]，王 彬[1]，吕 超[1]，王新南[2]，李 星[3]，朱知寿[2]，候慧龙[1,4]，赵新青[1]

1. 北京航空航天大学 材料科学与工程学院，北京 100191；
2. 中国航空发动机集团 北京航空材料研究院 先进钛合金重点实验室，北京 100095；
3. 南京理工大学 先进金属与金属间化合物材料技术工信部重点实验室，南京 210094；
4. 天目山实验室(航空浙江省实验室)，杭州 311312

摘 要：采用光学显微镜(OM)、扫描电子显微镜(SEM)、背散射电子衍射(EBSD)和高角度环形暗场扫描透射电子显微镜(HAADF-STEM)研究 Ti−6Al−4V 和 Ti−6.5Al−2Zr−1Mo−1V 合金中 Burgers 位相关系(BOR)的角度偏差和影响因素。引入球心角模型计算 α 和 β 相的位相与理想 BOR 之间的角度偏差。研究结果表明，在 $\beta\rightarrow\alpha$ 相变过程中，两种合金中 α 集束内的 α 相和 β 相不遵循理想的 BOR，且角度偏差值小于 3°。通过详细的显微组织表征发现，沿两个不同入射电子方向观察到 α/β 界面呈原子尺度的阶梯状结构特征，并在 α 和 β 相内部以及 α/β 界面附近观察到大量位错。进一步研究表明，角度偏差主要源于 α 和 β 相中位错引起的晶格畸变以及 α/β 界面的晶格错配。

关键词：钛合金；Burgers 位相关系；角度偏差；α/β 界面；位错；晶格畸变

(Edited by Wei-ping CHEN)